HAL open science

Numerical simulations of three MAP IOPs and associated microphysical processes

Franck Lascaux, Evelyne Richard, Jean-Pierre Pinty

To cite this version:

Franck Lascaux, Evelyne Richard, Jean-Pierre Pinty. Numerical simulations of three MAP IOPs and associated microphysical processes. Quarterly Journal of the Royal Meteorological Society, 2006, 132 (619), pp.1907-1926. 10.1256/qj.05.197 . hal-00138156

HAL Id: hal-00138156

https://hal.science/hal-00138156v1

Submitted on 14 Sep 2021

HAL is a multi-disciplinary open access archive for the deposit and dissemination of scientific research documents, whether they are published or not. The documents may come from teaching and research institutions in France or abroad, or from public or private research centers.

L'archive ouverte pluridisciplinaire **HAL**, est destinée au dépôt et à la diffusion de documents scientifiques de niveau recherche, publiés ou non, émanant des établissements d'enseignement et de recherche français ou étrangers, des laboratoires publics ou privés.

Distributed under a Creative Commons Attribution 4.0 International License

Numerical simulations of three different MAP IOPs and the associated microphysical processes

By FRANCK LASCAUX*, EVELYNE RICHARD and JEAN-PIERRE PINTY
Laboratoire d'Aérologie, CNRS/UPS, France

SUMMARY

The data collected during three contrasting Intensive Observing Periods (IOPs) of the Mesoscale Alpine Programme (MAP) were used to assess the performance of the Meso-NH model with particular emphasis on precipitation and microphysical processes. The model was able to reproduce the intense and moderate convective rain of IOPs 2A and 3, respectively, and also the stratiform precipitation associated with IOP 8. Microphysical budget computations were used to derive the mean vertical distribution of the hydrometeors and to quantify the relationships among the different water species. The results of IOP 8 exhibit a shallow stratiform system in which the dominant ice hydrometeor is snow, growing efficiently by vapour deposition. In contrast, the results of IOP 2A show a much deeper system in which graupel and its associated growth modes play an important role. These results are consistent with the two conceptual models of orographic rain that were derived from the MAP radar observations.

KEYWORDS: High-resolution simulation Mesoscale Alpine Programme

1. INTRODUCTION

Like most of the major mountain ranges, the European Alps exert a strong influence on the space and time distribution of precipitation. In particular, during autumn, heavy rainfalls and consequent flash floods (e.g. Doswell *et al.* 1996) frequently occur on the southern side of the Alps, linked to the passage of a baroclinic trough coming from the west (Massacand *et al.* 1998). These heavy precipitation events are often inaccurately forecast and can be very devastating. For instance, floods over northern Italy on 14 October 2000 resulted in 37 casualties and 450 million US dollars in damage. To improve the understanding and forecasting of these events was one of the central objectives of the Mesoscale Alpine Programme (MAP). The two-month Special Observing Period (SOP) of MAP, held in the autumn of 1999, provided detailed documentation on several major rain events over the southern Alps (Bougeault *et al.* 2001; Volkert 2005 and references therein).

In recent years, the field of short-range precipitation forecasting has undergone major development with the emergence and consolidation of new numerical models solving the full non-hydrostatic set of equations and thus being able to explicitly resolve moist convection. The development of these new models was accompanied by a substantial refinement of most physical parametrizations, and especially those devoted to the explicit representation of clouds and precipitation. In this context, the MAP dataset offered a unique opportunity to test, validate and improve these new high-resolution numerical tools (see Richard *et al.* 2005 for a short review).

In this study, the data collected during three Intensive Observing Periods (IOPs) of MAP are used to assess the performance of the Meso-NH model with particular emphasis on precipitation and microphysical processes. The study is focused on the Lago Maggiore MAP target area for which many radar observations are available and have been processed and analysed in previous studies. Among these data, the cloud microphysics retrievals—deduced from the S-band dual-polarized (S-Pol) radar

* Corresponding author: Laboratoire d'Aerologie UMR 5560, Observatoire Midi-Pyrenees, 14 Avenue Edouard Belin, 31400 Toulouse, France. e-mail: lasf@aero.obs-mip.fr

observations and based upon the fuzzy-logic method of Vivekanandan *et al.* (1999)—are particularly valuable.

The three IOPs selected represent contrasting situations. All of them are associated with an upper-level trough moving eastwards with southerly low-level moist flow pointing towards north-west Italy. However, the associated precipitation was notably different: intense and moderate convection for IOPs 2A and 3 respectively, and widespread stratiform rain for IOP 8. These three cases were simulated with the Meso-NH model with the aim of addressing the following questions:

- Is the model able to reproduce the occurrence, location, and intensity of the observed precipitation?
- Is the vertical distribution of the hydrometeors correctly captured?
- What are the important microphysical pathways and how do they differ from one case to another?
- Are they consistent with the conceptual models of orographic precipitation derived from the MAP observations by Medina and Houze (2002)?

The paper is organized as follows. Section 2 provides a description of the model experimental design and analysis method. Sections 3, 4, and 5 are respectively devoted to the IOP 2A, 3 and 8 model results which are compared with the available observations. The microphysical process studies are presented in section 6. A discussion and summary are given in the final section.

2. Model description

(*a*) *Numerical set-up*

The numerical simulations were conducted with the French Meso-NH model (Lafore *et al.* 1998) developed at Centre National de Recherches de la Météorologie (CNRM) and Laboratoire d'Aérologie (LA). The Meso-NH model solves a non-hydrostatic system of equations based upon the Lipps and Hemler (1982) anelastic formulation. The vertical coordinate follows Gal-Chen and Sommerville (1975). A C-grid in the formulation of Arakawa and Messinger (1976) is used for the spatial discretization and the temporal scheme is an explicit leapfrog scheme with a time filter (Asselin 1972). In this study, three interactively 2-way nested domains (Stein *et al.* 2000) were used with horizontal mesh sizes of 32, 8, and 2 km. The area corresponding to the coarsest domain (D1) is shown in Fig. 1(a) together with the location of the nested domains (D2 and D3). D1 covers the synoptic conditions over western Europe, D2 covers the entire Alpine massif, and D3 is centred above the Lago Maggiore area. The topography of the innermost domain is shown in Fig. 1(b). Subgrid-scale convection is parametrized for horizontal resolutions of 32 and 8 km by a mass-flux convection scheme (Bechtold *et al.* 2001), whereas for the 2 km inner grid convection is explicitly resolved.

The initial and boundary conditions used for the simulations of MAP IOPs 3 and 8 were taken from the MAP European Centre for Medium-range Weather Forecasts (ECMWF) re-analyses (extensively described in Keil and Cardinali 2004). For the case of MAP IOP 2A, the ECMWF operational analyses were preferred to the MAP re-analyses since previous studies (Richard *et al.* 2001; Lascaux *et al.* 2004) had shown, for this particular event, a strong sensitivity to the initial conditions and the detrimental effect of the MAP re-analyses.

The beginning and ending times of each simulation are indicated in Table 1. IOP 2A was a short event (the simulation lasted only 18 hours), whereas the simulations of IOPs 3 and 8 were both integrated over 36 hours.

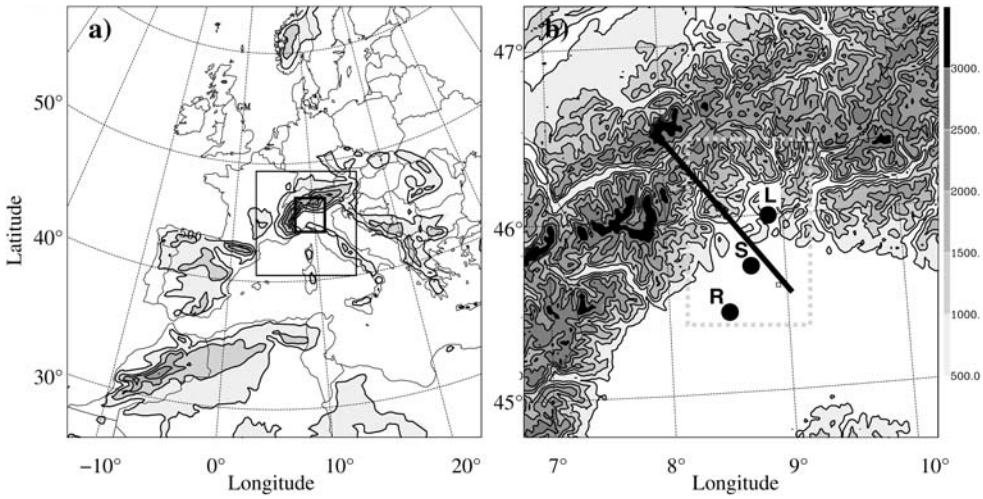

Figure 1. (a) Geographical domains used for the nested simulation. The outer frame shows the 32 km grid-mesh domain and its topography; the location of the 8 km (2 km) grid-mesh domain is indicated by the thin (bold) square. (b) Topography (m) of the 2 km grid-mesh domain, and locations of the three radars (R, S, and L for Ronsard, S-Pol, and Monte Lema respectively). The dashed square denotes the subdomain used for the microphysical budget computation and the bold solid line indicates the location of the vertical cross-section shown in Fig. 7.

TABLE 1. SIMULATION DATES AND TIMES

Event	Simulation start	Budget computation start	Simulation end
IOP 2A	1200 UTC 17 Sep	2000 UTC 17 Sep	0600 UTC 18 Sep
IOP 3	1200 UTC 25 Sep	1830 UTC 25 Sep	0000 UTC 27 Sep
IOP 8	1200 UTC 20 Oct	1700 UTC 21 Oct	0000 UTC 22 Oct

The budget computations were carried out over a 15 min period.

(*b*) *Microphysical scheme*

All the simulations make use of an explicit bulk microphysical scheme. In the first two domains, the microphysical scheme (referred to as ICE3; Pinty and Jabouille 1998) predicts the time evolution of the mixing ratios of six water species: Rv (vapour), Rc (cloud droplets), Rr (raindrops), and Ri (pristine ice), Rs (snow/aggregates), and Rg (frozen drops/graupel), the three ice species being ordered by increasing degree of riming. This scheme has been recently extended to account for hail particles. The new scheme (referred to as ICE4; Pinty *et al.* 2002) is used only in the inner domain. It includes an additional prognostic variable for the hail mixing ratio, Rh. Hail particles, fed by the wet growth of the graupel, have specific microphysical properties. Compared to graupel, hail is denser, falls faster and is a more efficient collector to wash out supercooled water and small ice crystals. This extension of the scheme was motivated by the previous study by Richard *et al.* (2003) which showed that, in the case of IOP 2A (for which a significant amount of hail was observed), the model results were quite sensitive to the assumptions made to describe the most heavily rimed particles of ICE3 (i.e. whether they were considered as hail-like particles rather than as graupel-like particles).

Figure 2 provides a sketch of the numerous interactions operating between the different water species and Table 2 gives a comprehensive list of the microphysical processes which are taken into account. More details about the ICE3 and ICE4 microphysical schemes are given in the appendix.

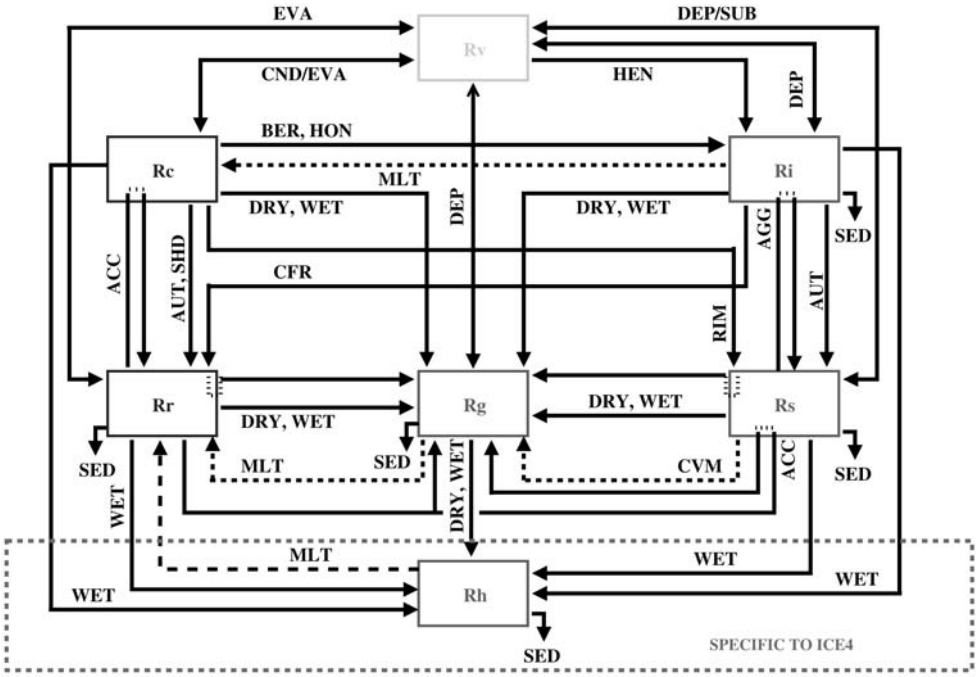

Figure 2. Sketch of the ICE3 and ICE4 microphysical schemes. Rv, Rc, Rr, Ri, Rs, Rg, and Rh refer to the mixing ratios of water vapour, cloud droplets, raindrops, pristine ice, snow/aggregates, graupel, and hail respectively. The different microphysical processes are designated by a group of three letters (EVA, DEP, etc.; see Table 2 for the complete list).

(*c*) *Budget computation*

An important tool for this study was the calculation of a full microphysical budget. By quantifying the relationships among water species, one can determine which microphysical processes contribute most to the production and destruction of a specific hydrometeor species. The budget computations were performed in a subdomain centred over the Lago Maggiore area (see Fig. 1(b)). This subdomain is common to the three IOPs and approximately half the grid points are located over the plain and half over the mountains. The budget was integrated over 15-minute time periods as indicated in Table 1. These time periods were selected to be representative of the mature phase of each event. The budget computation will be used to derive the mean vertical distribution (averaged horizontally and over time) of the different mixing ratios and associated microphysical processes.

3. IOP 2A

(*a*) *Synoptic situation*

IOP 2A was characterized by the propagation of an intense convective system above the Lago Maggiore area. Precipitation rates of 70 mm in six hours were observed and high reflectivity cores in the radar observations (>60 dBZ at 6 km) revealed the presence of hail in significant amounts (Tabary *et al.* 2002).

The ECMWF analysis was used to describe the meteorological situation at 12 UTC on 17 September 1999 (Figs. 3(a) and (b)). At the surface, a 982 hPa low was located 15° west of Ireland. The associated large-scale cyclonic structure was moving eastwards towards Europe. A secondary low (1004 hPa) above the Italian peninsula generated a

TABLE 2. MICROPHYSICAL PROCESSES

Symbol	Mechanism	Sink	Source	Process
V-HEN-I	$Rv \Rightarrow Ri$	Rv	Ri	Heterogeneous nucleation
C-HON-I	$Rc \Rightarrow Ri$	Rc	Ri	Homogeneous nucleation
R-HON-G	$Rr \Rightarrow Rg$	Rr	Rg	Homogeneous nucleation
C-BER-I	$Rc \Rightarrow Ri$	Rc	Ri	Bergeron-Findeisen effect
V-DEP-I	$Rv + Ri \Rightarrow Ri$	Rv	Ri	Deposition (Sublimation)
V-DEP-S[d]	$Rv + Rs \Rightarrow Rs$	Rv	Rs	Deposition (Sublimation)
V-DEP-G[d]	$Rv + Rg \Rightarrow Rg$	Rv	Rg	Deposition (Sublimation)
V-CND-C	$Rv \Rightarrow Rc$	Rv	Rc	Condensation (Evaporation)
C-AUT-R[g]	$Rc + Rc \Rightarrow Rr$	Rc	Rr	Autoconversion of cloud droplets
I-AUT-S[c]	$Ri + Ri \Rightarrow Rs$	Ri	Rs	Autoconversion of pristine ice
I-AGG-S[c]	$Ri + Rs \Rightarrow Rs$	Ri	Rs	Aggregation of pristine ice
R-CFR-(I)G	$Ri + Rr \Rightarrow Rg$	Rr	Rg	Raindrop contact freezing
I-CFR-(R)G	$Ri + Rr \Rightarrow Rg$	Ri	Rg	Raindrop contact freezing
C-RIM-S[b]	$Rc + Rs \Rightarrow Rs$	Rc	Rs	Light riming of aggregates
C-RIM-(S)G[b]	$Rc + Rs \Rightarrow Rg$	Rc	Rg	Heavy riming of aggregates
S-RIM-(C)G	$Rc + Rs \Rightarrow Rg$	Rs	Rg	Heavy riming of aggregates
C-ACC-R[f]	$Rc + Rr \Rightarrow Rr$	Rc	Rr	Accretion of rain and cloud droplets
R-ACC-(S)G[e]	$Rr + Rs \Rightarrow Rg$	Rr	Rg	Accretion of rain and aggregates
S-ACC-(R)G	$Rr + Rs \Rightarrow Rs$	Rs	Rg	Accretion of rain and aggregates
C-DRY-G[a]	$Rc + Rg \Rightarrow Rg$	Rc	Rg	Dry growth of graupel
R-DRY-G[a]	$Rr + Rg \Rightarrow Rg$	Rr	Rg	Dry growth of graupel
I-DRY-G[a]	$Ri + Rg \Rightarrow Rg$	Ri	Rg	Dry growth of graupel
S-DRY-G	$Rs + Rg \Rightarrow Rg$	Rs	Rg	Dry growth of graupel
C-SHD-(G)R	$Rc + Rg \Rightarrow Rr$	Rc	Rr	Water shedding
C-WET-G	$Rc + Rg \Rightarrow Rg$	Rc	Rg	Wet growth of graupel
R-WET-G	$Rr + Rg \Rightarrow Rg$	Rr	Rg	Wet growth of graupel
I-WET-G	$Ri + Rg \Rightarrow Rg$	Ri	Rg	Wet growth of graupel
S-WET-G	$Rs + Rg \Rightarrow Rg$	Rs	Rg	Wet growth of graupel
S-WET-(G)H	$Rs + Rg \Rightarrow Rh$	Rs	Rh	Hail formation
G-WET-(S)H	$Rs + Rg \Rightarrow Rh$	Rg	Rh	Hail formation
C-WET-H	$Rc + Rh \Rightarrow Rh$	Rc	Rh	Wet growth of hail
R-WET-H	$Rr + Rh \Rightarrow Rh$	Rr	Rh	Wet growth of hail
I-WET-H	$Ri + Rh \Rightarrow Rh$	Ri	Rh	Wet growth of hail
S-WET-H	$Rs + Rh \Rightarrow Rh$	Rs	Rh	Wet growth of hail
G-WET-H	$Rs + Rg \Rightarrow Rh$	Rs	Rh	Wet growth of hail
I-MLT-C	$Ri \Rightarrow Rc$	Ri	Rc	Melting of pristine ice
G-MLT-R[i]	$Rg \Rightarrow Rr$	Rg	Rr	Melting of graupel
H-MLT-R[i]	$Rh \Rightarrow Rr$	Rh	Rr	Melting of hail
S-CVM-G	$Rs \Rightarrow Rg$	Rs	Rg	Conversion melting
R-EVA-V[h]	$Rr \Rightarrow Rv$	Rr	Rv	Rain evaporation

List of the microphysical processes and corresponding sinks and sources. In the symbol names, the first letter identifies the sink species (V, C, I, R, S, G, or H for vapour, cloud, pristine ice, rain, snow, graupel, or hail respectively), the next three letters give the short name of the microphysical process, and the last letter identifies the source species. An optional letter is added in parenthesis to recall the name of the reactant species in three-component processes. Superscripts ([a],[b], etc.) indicate groupings used in Fig. 13.

10 m s^{-1} flow above the Adriatic towards north-western Italy. At 500 hPa, a ridge elongated over north-eastern Europe from Hungary to Scandinavia and a trough from Ireland to southern Spain. Between these two features, a short-wave trough over southern France was propagating eastwards. As a consequence, the atmosphere above northern Italy was destabilized by advection of cold moist air in the middle levels as shown in Figs. 4(a) and (b), displaying the evolution of the Milano-Linate radiosounding between 12 and 18 UTC.

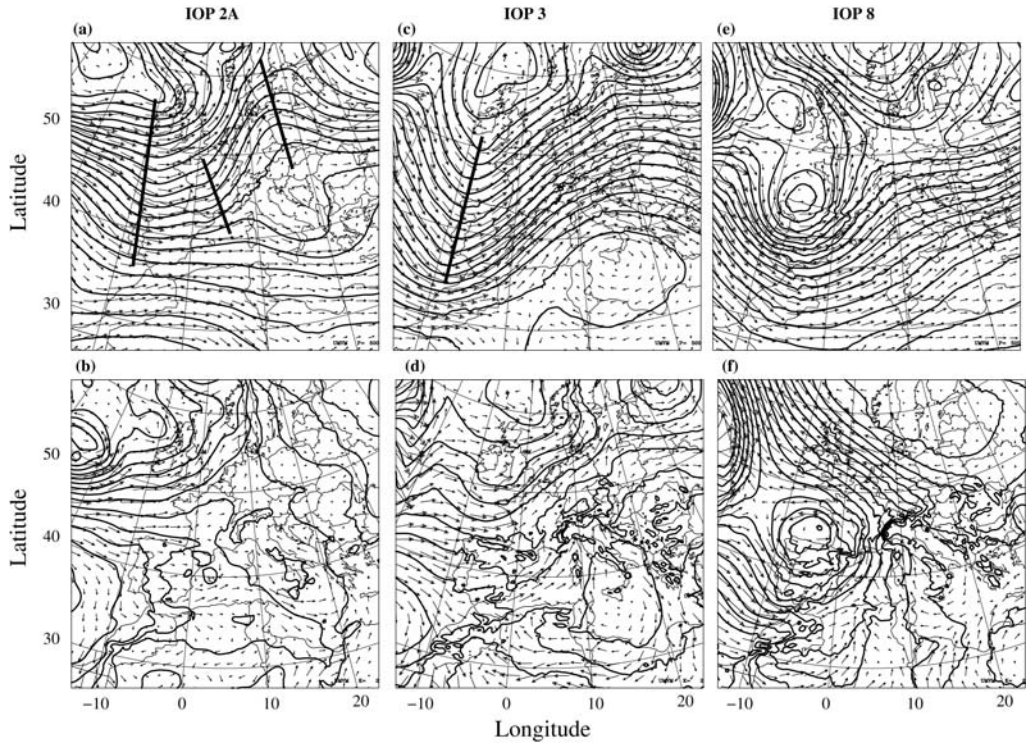

Figure 3. Synoptic situation at 12 UTC on 17 September 1999 (IOP 2A): (a) 500 hPa geopotential height (contour interval 30 m) with wind vectors, and (b) mean-sea-level pressure (contour interval 3 hPa) with surface wind vectors. (c, d) and (e, f) are as (a, b), but for 12 UTC on 25 September 1999 (IOP 3) and on 20 October 1999 (IOP 8), respectively. The bold lines in (a) and (c) indicate the locations of the troughs or ridges mentioned in the text.

The mean vertical profile of the equivalent potential temperature, computed for Milano-Linate during the first ten hours of the simulation and plotted in Fig. 5, confirms the strong instability during IOP 2A.

(*b*) *Reflectivity fields*

Observations of reflectivity over the Lago Maggiore region were provided by a ground-based Doppler radar network composed of three radars: the S-Pol polarimetric radar from the US National Center for Atmospheric Research, the French C-band research radar Ronsard and the MeteoSwiss C-band operational radar located at Monte Lema. Composite reflectivity fields were obtained by interpolating the three radar fields on a 2 km $\times$ 2 km $\times$ 500 m grid and by retaining the maximum value of the three radar observations.

The time evolution of the composite radar reflectivity at 2000 m is shown in the top row of Fig. 6. During the first hours of the simulation (from 12 to 18 UTC, not shown) only isolated cells developed over the first slopes of the Alps. Between 18 and 20 UTC, these cells merged into a well-defined convective line which started to propagate south-eastwards. In the evening (21 UTC), the system became more complex with further convection developing ahead of the initial line. After 00 UTC, the system left the observation area and satellite observations showed that it decayed fast.

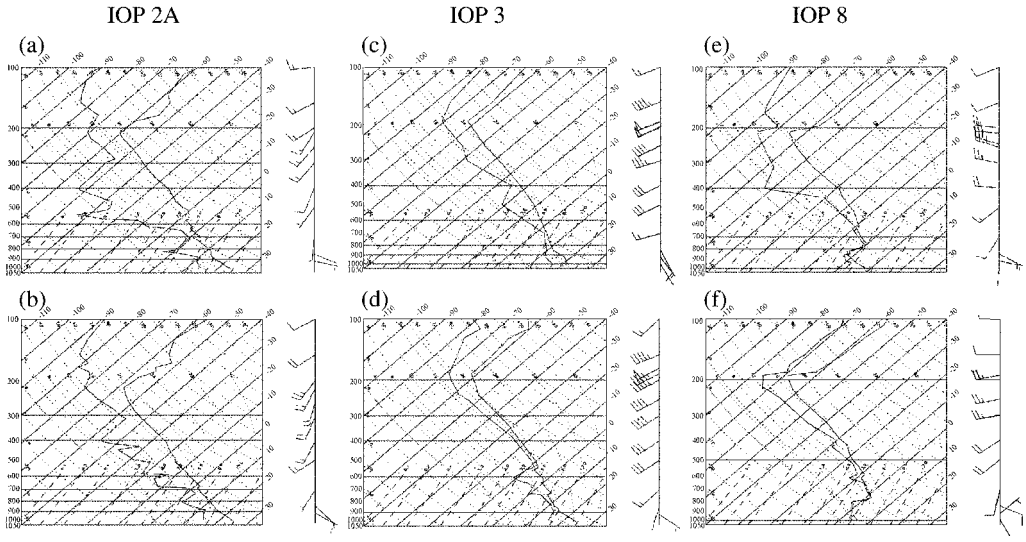

Figure 4. Milano radiosoundings for IOP 2A (17 September 1999) at (a) 12 UTC and (b) 18 UTC. (c, d) and (e, f) are as (a, b), but for IOP 3 (25 September 1999) and IOP 8 (20 October 1999), respectively.

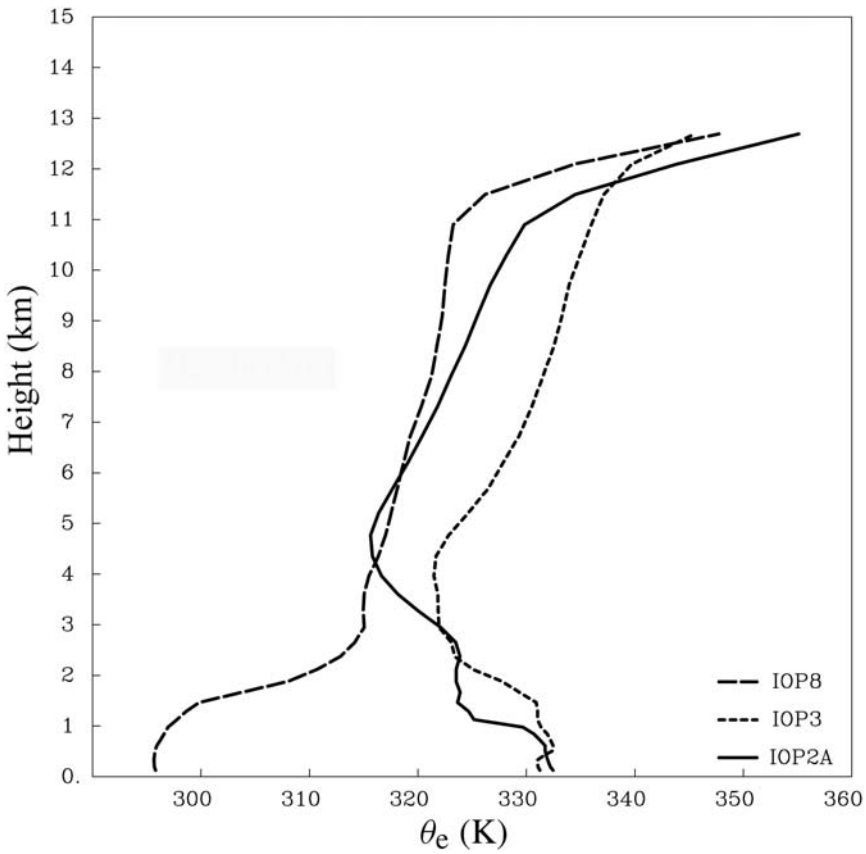

Figure 5. Mean vertical profile of the equivalent potential temperature for IOP 2A, IOP 3, and IOP 8 at Milano-Linate computed in the model and averaged over the first ten hours of each simulation.

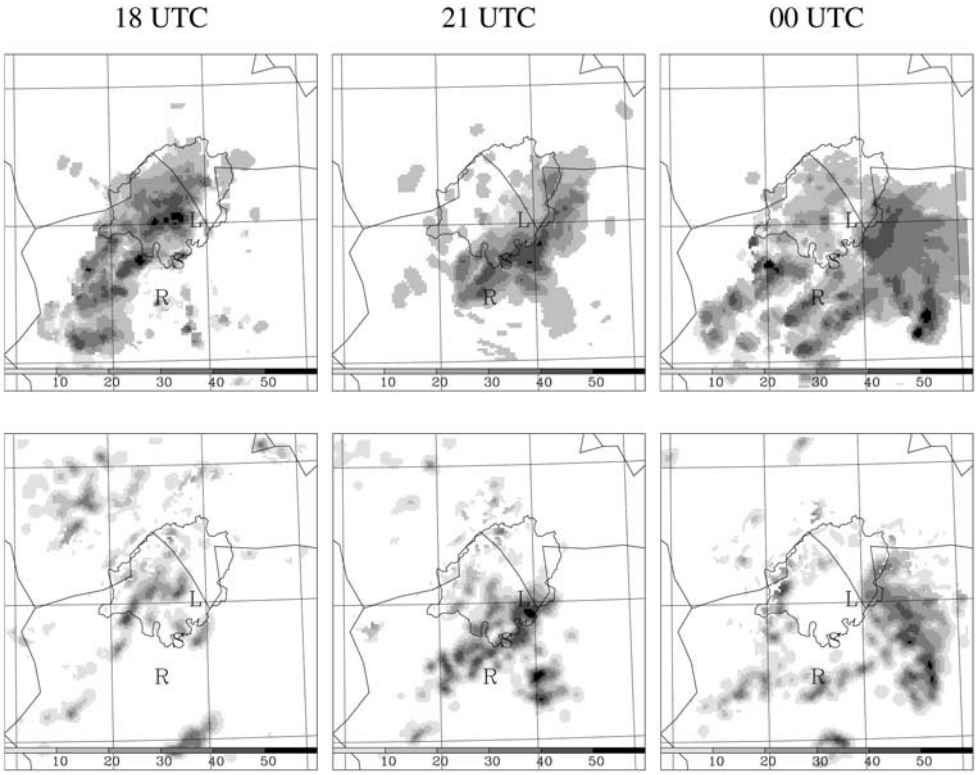

Figure 6. Time evolution of the radar reflectivity (dBZ) at 2000 m for IOP 2A from 18 UTC on 17 September to 00 UTC on 18 September. The upper row shows observed fields from the radar composite, and the lower row the results from the simulation. The closed contour indicates the limits of the Toce-Ticino watershed. The other lines approximately represent the borders between France, Italy and Switzerland. The locations of the Monte Lema, S-Pol and Ronsard radars are indicated by the letters L, S, and R respectively.

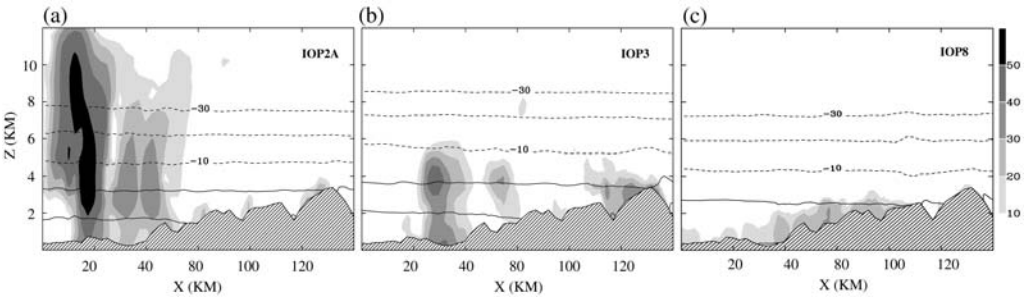

Figure 7. Vertical cross-section of the simulated radar reflectivity (shading, dBZ) and temperature (contours, °C) along the line shown in Fig. 1(b) for (a) IOP 2A (2000 UTC on 17 September 1999), (b) IOP 3 (1830 UTC on 25 September 1999), and (c) IOP 8 (1700 UTC on 21 October 1999).

The time evolution of the equivalent radar reflectivity computed from the model fields (see Richard *et al.* 2003 for the detail of the computation) is displayed in the bottom row of Fig. 6. Even though the spatial extent of the simulated system appears underestimated, the model succeeds reasonably well in reproducing the development of the convective cells and their merging into a convective line propagating south-eastwards. Even the further evolution into a three-dimensional system is captured.

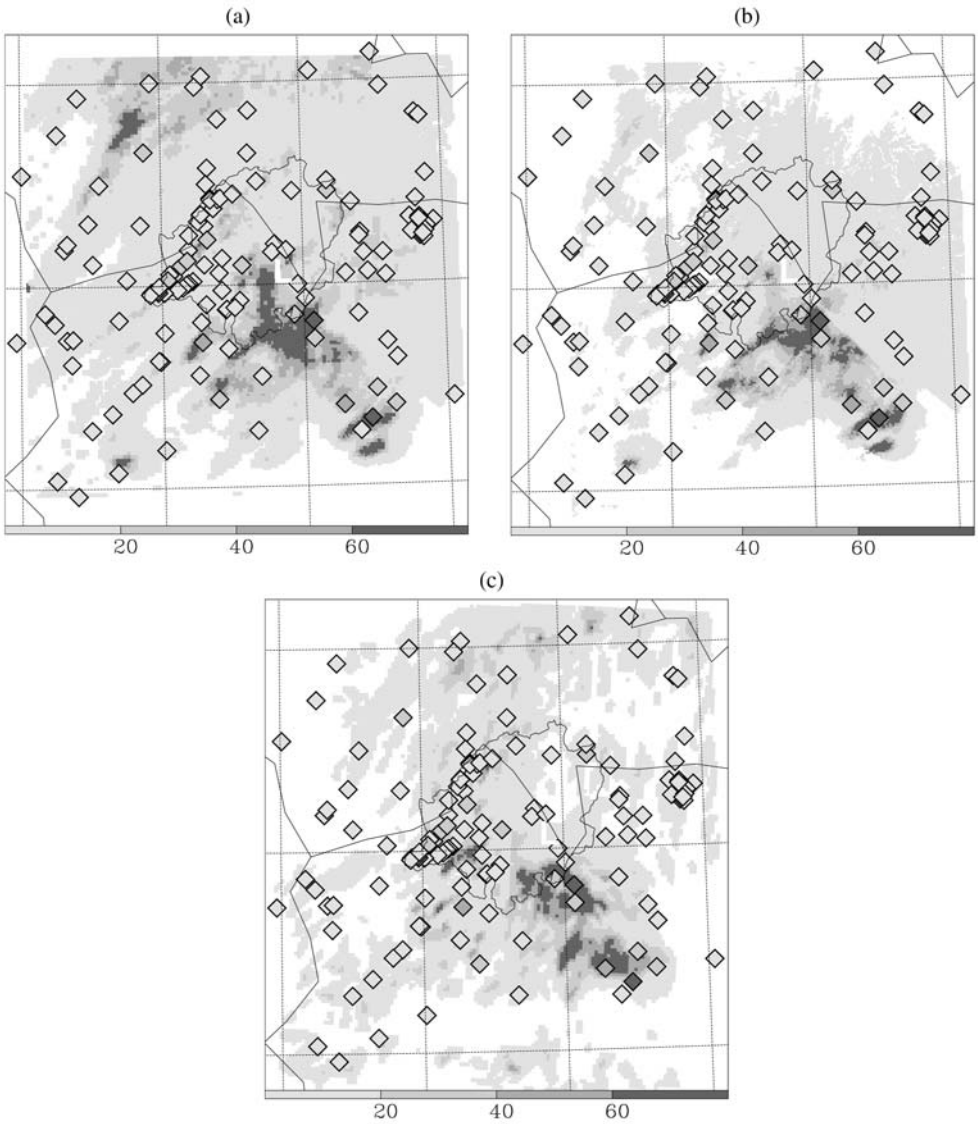

Figure 8. 12-hour accumulated precipitation (shading, mm) from 12 UTC on 17 September 1999 (a) deduced from the Alpine radar composite, (b) deduced from the RAIN data product, and (c) computed in the 2 km grid-mesh domain. The corresponding raingauge measurements (diamonds) are superimposed on each plot.

A vertical cross-section of the simulated reflectivity field (Fig. 7(a)) shows quite a deep system with cloud tops reaching 12 km and reflectivity values exceeding 50 dBZ up to 10 km. These features are in agreement with the radar observations described in Tabary *et al.* (2002).

(*c*) *Precipitation fields*

The ALPRAD precipitation fields taken from Richard *et al.* (2003) were used to assess the IOP 2A simulation above the Lago Maggiore area. These fields were derived from the Alpine radar composite of Hagen (1999) but are available only for a limited

period of the MAP SOP. Figure 8(a) shows the ALPRAD precipitation accumulated over 12 hours from 12 UTC on 17 September 1999. The model precipitation field (innermost domain, 2 km resolution) accumulated over the same period is displayed in Fig. 8(c). On both fields, the corresponding raingauge measurements are superimposed. The location of the wide precipitation maximum observed in the south-east of the domain (precipitation rates higher than 40 mm in 12 hours) is well captured by the model. However, the narrow precipitation band present in the north-west of the domain does not appear in the simulation. Another estimation of the surface rainfall was deduced from the RAIN product of the Monte Lema radar (Germann and Joss 2000). This product is available from the MAP data centre for the whole MAP SOP but needs to be calibrated with raingauge measurements. For this IOP, a multiplying factor of 2 was found to give the best fit between the RAIN data and the raingauge measurements. Figure 8(b) shows the 12-hour accumulated precipitation deduced from the RAIN data. When compared to the ALPRAD field over the same period, it is clear that precipitation north of Monte Lema is poorly observed by the radar in the RAIN product. It is important to bear this in mind, especially when looking at the other two IOPs for which the RAIN product is the only one available.

4. IOP 3

(*a*) *Synoptic situation*

The IOP 3 event was characterized by continuous orographic precipitation above Lago Maggiore and the first south-facing slopes of the Alps, with observed precipitation rates exceeding 300 mm in 48 hours. A detailed study of this case can be found in Pujol *et al.* (2005).

The 500 hPa geopotential chart from the ECMWF re-analysis of 12 UTC on 25 September (Fig. 3(c)) shows an elongated trough lying over the Atlantic Ocean from west of Morocco to north of Scotland, inducing a south-westerly flow over the western Mediterranean. At low levels (Fig. 3(d)), the south-westerly flow encountered the mountains north of Lago Maggiore and this led to the formation of convective cells. This flow continued during the whole IOP. At 12 UTC on 25 September, the Milano-Linate radiosounding (Fig. 4(b)) shows a layer of warm and wet, potentially unstable air extending from the ground to 700 hPa.

The mean vertical profile of the equivalent potential temperature computed in the model (Fig. 5) at Milano/Linate on 25 September confirms the potential instability of the event. The air is stable in the lowest layers and becomes unstable above approximately 500 m.

(*b*) *Reflectivity fields*

Observed values of radar reflectivity were derived from the same radar composite as the one used for IOP 2A. Reflectivity fields at 2000 m are plotted in the top row of Fig. 9 between 18 and 20 UTC on 25 September. The system was still active on 26 September but the corresponding reflectivities are not shown here. Convective cells were first initiated over the plain, merged when reaching the first slopes of the Lago Maggiore mountains and finally released their water content.

The equivalent radar reflectivities computed from the model are shown on the bottom row of Fig. 9. As for IOP 2A, the horizontal extent of the low reflectivities is underestimated in the model. However, the reflectivity maxima associated with the convective cells are well reproduced. In the evening of 25 September and in the morning of 26 September, the convective activity persisted over the mountains leading to a

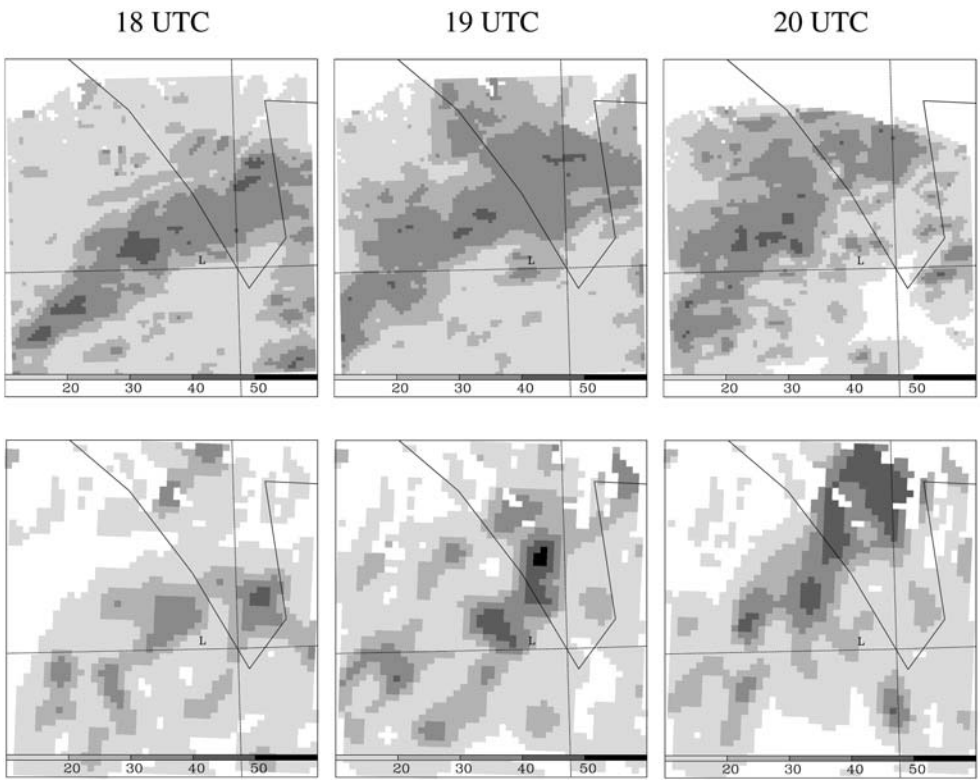

Figure 9. As Fig. 6, but over a smaller domain centred above the Lago Maggiore area and for IOP 3 (18 to 20 UTC on 25 September).

significant amount of accumulated precipitation. The convective system was not as deep as in IOP 2A. The vertical cross-section of the computed reflectivity at 1830 UTC on 25 September, shown in Fig. 7(b), indicates that cloud tops remained beyond 6000 m, which is consistent with the observations shown in Pujol *et al.* (2005).

(*c*) *Precipitation fields*

The RAIN product of Monte Lema was used to compare observations and model results. Figure 10 shows the 24-hour accumulated precipitation fields from 12 UTC on 25 September, deduced from RAIN and computed in the innermost domain. Both fields exhibit an elongated precipitation pattern, oriented south-west/north-east, and located over the Ticino-Toce watershed. The precipitation from the model extends further to the north-east than the radar field. However, the model results are consistent with the rain-gauge measurements. As was mentioned in section 3(b), the Monte Lema radar may not see this region well.

5. IOP 8

(*a*) *Synoptic situation*

During IOP 8, a baroclinic cyclone and associated cold front passing south of the Alps produced persistent and widespread precipitation over northern Italy. However the accumulation amounts remained moderate with local maxima hardly reaching 100 mm over north-eastern Italy and not exceeding 60 mm over the Lago Maggiore area.

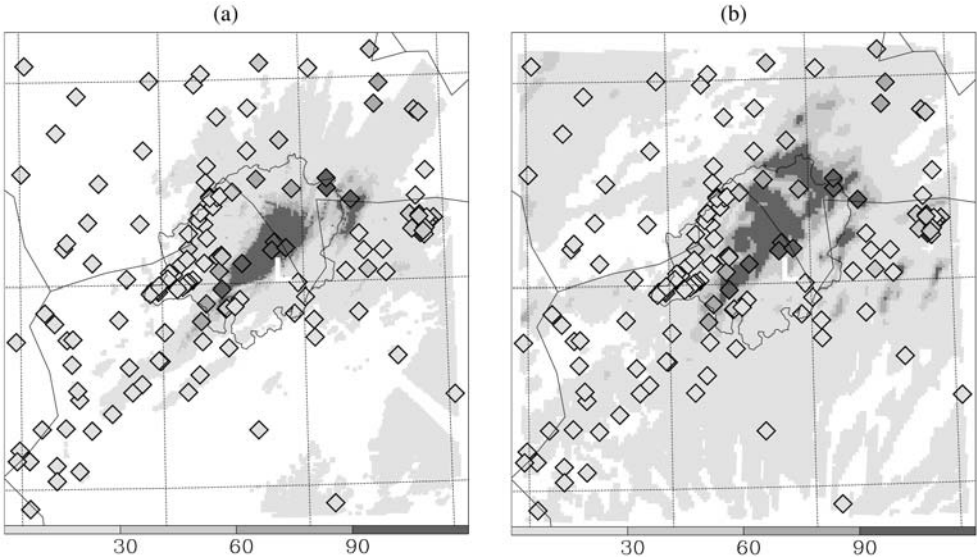

Figure 10. 24-hour accumulated precipitation (shading, mm) from 12 UTC on 25 September (a) deduced from the RAIN data product and (b) computed in the 2 km grid-mesh domain. L indicates the location of the Monte Lema radar.

The 500 hPa geopotential chart from the ECMWF re-analysis of 12 UTC on 20 October (Fig. 3(e)) shows a deep cut-off low located north of Spain and the corresponding surface chart (Fig. 3(f)) indicates a strong southerly flow impinging on the southern tip of the Alps and the Apennines. The Milano sounding (Fig. 4) reveals close-to-saturation conditions and stable stratification through the lowest few kilometres. The presence of a cold stable airmass over the Po valley (further evidenced in Fig. 5) has been outlined as a distinctive feature of IOP 8 in the previous studies dealing with this case (Bousquet and Smull 2003; Medina and Houze 2003; Rotunno and Ferretti 2003; Steiner *et al.* 2003).

(*b*) *Reflectivity fields*

Observed reflectivity values exhibited a mean stratiform structure with a bright band at 2 km. The reflectivity echoes remained weak (less than 20 dBZ for the S-Pol measurements averaged over the whole SOP; see Fig. 14(a) of Medina and Houze 2003) and less than 40 dBZ for the data collected on 21 October, around 0930 UTC, by the tail radar mounted aboard the NOAA P3 aircraft (see Fig. 5(a) of Bousquet and Smull 2003). The simulated reflectivities, shown in Fig. 7(c), are consistent with these observations. The strongest values (20 to 30 dBZ) are confined within the first two kilometres.

(*c*) *Precipitation fields*

The comparison was performed for the 24-hour precipitation derived from the RAIN product and accumulated from 00 UTC on 21 October (Fig. 11). For the IOP 8 event, possibly due to the stratiform character of the rain, a higher multiplying factor (equal to 6) was found necessary to obtain a reasonable match between the radar-deduced precipitation and the rain-gauge measurements. The radar field exhibits two maxima, one in the south of the Toce-Ticino watershed and a second one over the plain

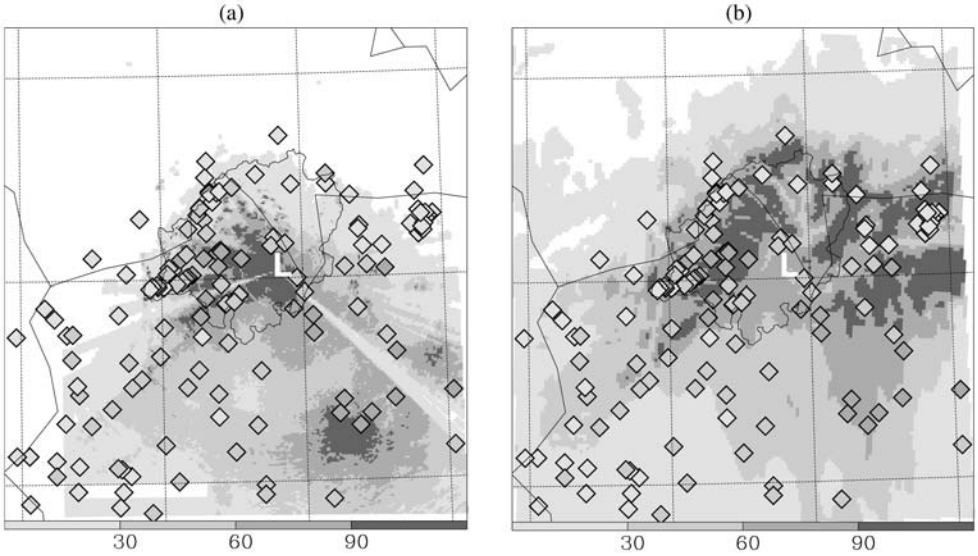

Figure 11. As Fig. 10, but for 00 UTC on 21 October to 00 UTC on 22 October.

in the southern part of the domain. In the model, the maximum over the Toce-Ticino watershed is misplaced by 20 to 30 km and the second maximum occurs too far north, more over the mountains than over the plain.

In terms of location, model results are not as good as for the other IOPs. The problem is already noticeable on the large-scale simulation (not shown), in which the model maximum over northern Italy is located too far east. A similar trend can be noted in the simulation performed with the MM5 model by Rotunno and Ferretti (2003). These contrasting performances between the three IOPs could indicate that the orographic forcing (much stronger in IOPs 2A and 3 than in IOP 8) may help to overcome the assumed lower predictability of convective situations relative to stratiform ones.

6. Hydrometeor distributions and dominant microphysical processes

In a study based upon the Monte Lema radar observations from autumn 1998 and 1999, Houze *et al.* (2001) found that the nature of the precipitation over the Lago Maggiore region is strongly dependent on the Froude number of the flow, *Fr*, which determines whether the flow is blocked or rises easily over the terrain. In a later study based on MAP IOPs 2B and 8 observations, Medina and Houze (2003) outlined fundamental microphysical differences between the unstable unblocked cases (low *Fr*, IOP 2B) and the stable blocked cases (high *Fr*, IOP 8). In the stable blocked case, precipitation is stratiform and essentially derives from the melting of snow. In the unstable unblocked case, rainfall is strongly enhanced via the orographic lifting of low-level moist air. Raindrop coalescence and graupel melting then become the dominant mechanisms in the rain production. In the following, the microphysical structure of the simulated cloud systems of IOPs 2A, 3, and 8 is examined with a view to investigating the extent to which the model results fit the conceptual models of orographic precipitation mechanisms proposed by Medina and Houze (2003).

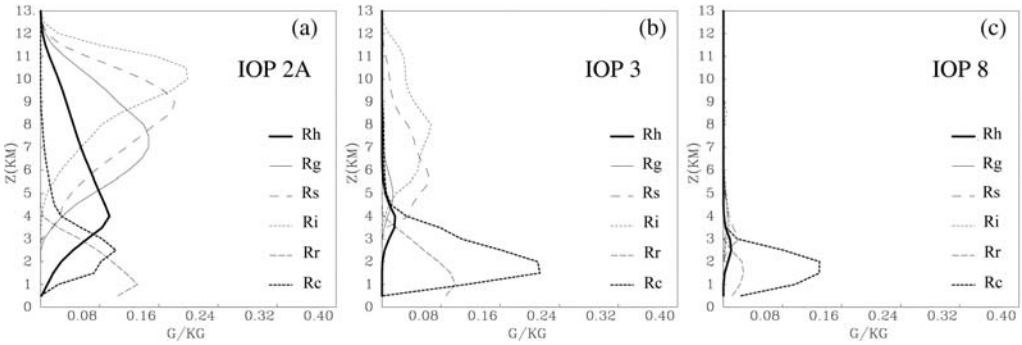

Figure 12. Mean vertical structure of the hydrometeors computed in the budget box shown in Fig. 1(b) for (a) IOP 2A, averaged between 2000 and 2015 UTC on 17 September 1999, (b) IOP 3, averaged between 1830 and 1845 UTC on 25 September 1999, and (c) IOP 8, averaged between 1700 and 1715 UTC on 20 October 1999. Rh, Rg, Rs, Ri, Rr, and Rc denote the mixing ratios of hail, graupel, snow/aggregates, pristine ice, rain water, and cloud water respectively.

(*a*) *Mean vertical structure of the hydrometeors*

To outline the mean vertical distribution of the hydrometeors for each MAP event, the temporal average of each hydrometeor mixing ratio was horizontally averaged (within the budget box defined in Fig. 1(b)) on constant height surfaces, with a vertical spacing of 500 m. As expected, the mean vertical profiles, displayed in Fig. 12, exhibit significant differences between the three IOPs.

As the convective system of IOP 2A has a considerable vertical extent (cloud tops exceed 10 km), large amounts of ice and snow are found at high levels. The pristine ice mean maximum (0.20 g kg^{-1}) is at approximately 10 km, and the snow/aggregates maximum (0.18 g kg^{-1}) is located one kilometre below. In comparison with IOP 2A, convection in IOP 3 is less intense and occurs mainly in isolated cells. As a consequence, maxima for pristine ice and snow/aggregates are located at lower elevations: 8 km for the former and 6 km for the latter. Moreover, these maxima (both equal to 0.08 g kg^{-1}) are much weaker. During IOP 2A, large amounts of graupel and hail are present above the freezing level with maximum values reaching 0.15 g kg^{-1} at 7000 m for graupel and 0.10 g kg^{-1} at 4000 m for hail. Graupel and hail are also present in IOP 3 , but only in very small amounts (less than 0.02 g kg^{-1} for the maxima found at 4000 m and 5000 m for hail and graupel, respectively). For both IOPs, the vertical layering of the simulated hydrometeors is quite consistent with the microphysical retrievals deduced from the S-Pol polarimetric observations. For IOP 2A, Tabary *et al.* (2002, see their Fig. 3) obtain a thick layer of hail after 20 UTC extending from 2 to 8 km, topped with a mixture of hail and graupel present up to 12 km. For IOP 3, Pujol *et al.*'s (2005) analysis (see their Fig. 14) reveals that the dominant hydrometeor type above the freezing level is dry snow found up to 7 to 8 km except in the most convective part of the system in which a mixture of hail and graupel appears between 4 and 5 km. For both IOPs, the amount of hail is, as expected, larger in the updraughts (for instance 0.45 g kg^{-1} in the updraughts versus 0.04 g kg^{-1} in the downdraughts on average for IOP 2A). This is also consistent with the radar retrievals.

During IOP 8, cloud tops hardly reach 5 km and all the hydrometeors are concentrated in the lower levels. Above the freezing level, the dominant particles are snow and aggregates. The mean snow maximum, 0.02 g kg^{-1}, is located at 3000 m.

In contradiction to the microphysical retrievals shown in Medina and Houze (2003), but in agreement with the results obtained in a later study (Houze and Medina 2005), some graupel is also present, embedded in the snow layer. The maximum (less than 0.01 g kg^{-1}) coincides with the melting level. In the model, below this level, the graupel production essentially results from the melting of the snow. During the melting process, it is assumed that a given portion of aggregates is converted into melting graupel at a rate representing the mixture of melted water and icy structures dense enough to be categorized as graupel. This type of graupel deriving from the melting snow should be compared with what the radar algorithm identifies as wet snow, which is usually not considered as a specific category in the model microphysical schemes. If we assimilate the melting graupel of the model to the wet snow retrieved from the polarimetric radar observations, the model results are in agreement with the IOP 8 observations and fairly well reproduce a shallow stratiform system in which the dominant ice hydrometeors are dry snow and wet snow.

(*b*) *Main microphysical processes*

In order to better understand the microphysical pathways operating in the three different cases, the vertical profiles of the most significant microphysical processes (averaged over time and horizontally) have been plotted in Fig. 13. The main microphysical tendencies acting on the liquid (rain) and solid (sum of snow, graupel and hail) precipitation are plotted on the bottom and top rows respectively. In each case, they have been normalized by the amount of corresponding precipitation, to better visualize what happens in the upper part of the cloud where the precipitation is weak, as in the case of IOPs 3 and 8.

In the case of IOP 8, the main processes leading to solid precipitation are snow growth by autoconversion and aggregation of pristine ice (AUG = AUT + AGG) together with vapour deposition (DEP) acting within the same height layer (4 to 6 km) and almost in the same proportion. In a thin layer above the freezing level, riming (RIM) takes over to further increase the amount of snow. All other processes remain weak. Below the freezing level, rain formation essentially results, first from snow melting (main contribution to MLT via the conversion-melting process CVM), and then from the accretion of cloud droplets (ACC-R). This scenario is consistent with Medina and Houze's conceptual model for the blocked stable case. Vapour diffusion onto snow particles (dominant term in DEP) plays an important role and snow melting makes a large contribution to the low-level precipitation.

IOP 3 is representative of moderate convection embedded in a stratiform background. Therefore, typical processes occurring in stratiform precipitation are also present, autoconversion/aggregation of pristine ice and snow riming above the freezing level, and snow melting and cloud accretion below. However, IOP 3 differs from IOP 8 in the sense that vapour deposition makes a weaker contribution than in IOP 8. Snow growth in the upper part of the cloud essentially derives from autoconversion and aggregation of pristine ice.

In the case of IOP 2A, other processes become important. First, the riming of snow occurs over a much deeper layer (between 4 and 9 km) and is dominated by the contribution of heavy riming. In the model, the distinction between heavy and light riming depends on the size of the rimed particles. If smaller than 7 mm in diameter, the particles are still considered as snow/aggregates (light riming), but larger than this threshold value they are converted into graupel (heavy riming).

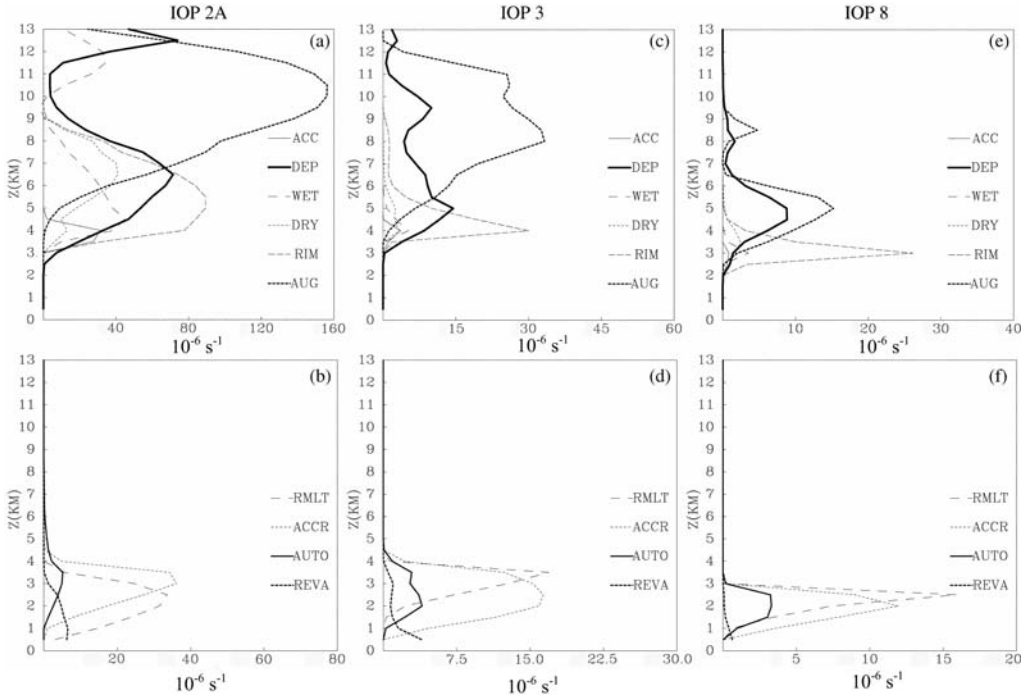

Figure 13. Mean vertical structure of the main microphysical processes involved in IOP 2A; normalized sources acting on (a) the solid precipitation ($Rs + Rg + Rh$, see text) with groupings DRY^a, RIM^b, AUG^c, DEP^d and ACC^e, and on (b) the liquid precipitation (Rr) with ACCR^f, AUTO^g, REVA^h, RMLT^i. Groupings are formed from processes marked by corresponding superscripts in Table 2. The averaging periods are the same as in Fig. 12. (c, d) and (e, f) are as (a, b), but for IOPs 3 and 8, respectively.

Then two other processes have significant contributions: dry growth of graupel (DRY), peaking at 7 km, and wet growth of graupel and hail (WET), constantly increasing from 9 km down to the melting level. Within the melting layer, the solid precipitation grows further by collecting raindrops. As in IOPs 3 and 8, melting and cloud droplet accretion dominate the generation of liquid precipitation but melting now essentially originates from graupel and hail and, owing to the larger size of these particles, it occurs at a comparatively lower altitude. These results are consistent with Medina and Houze's conceptual model for the unblocked unstable case. Under such flow conditions, the lifting of moisture-laden, low-level air together with the occurrence of embedded convective cells brings enough cloud water above the freezing level to favour graupel production, first by snow riming, then by dry growth. As convection is quite intense in IOP 2A, not all the accreted water can freeze, and the wet growth processes take over close to the freezing level. This leads to the formation of substantial amounts of hail.

7. Conclusion

A variety of three MAP contrasting cases have been simulated with the French non-hydrostatic model Meso-NH in order to investigate the capability of the model to reproduce intense orographic precipitation and associated microphysical processes. These three events are characterized by different flow regimes. IOPs 2A and 3 exhibit

unstable and potentially unstable conditions respectively (with 'flow over'), whereas IOP 8 is characterized by stable conditions and blocked flow in the low levels.

The model succeeds quite well in reproducing the occurrence, location and intensity of the observed precipitation of IOPs 2A and 3, both on the large scale and on the gamma-mesoscale. More mixed results are found in the case of IOP 8. On the large scale, the simulated precipitation occurs too far east. Consequently the fine-scale precipitation in the Lago Maggiore region cannot be as accurately simulated as for IOPs 2A and 3. However, despite the positioning error, the microphysical scheme of the model is able to reproduce the stratiform character of the precipitation associated with IOP 8. Furthermore, the clear distinction between the three IOPs is well depicted: deep convection for IOP 2A (reaching 12 km), moderate convection for IOP 3 (not exceeding 6 km), and stratiform rain for IOP 8 (confined to the first 2 km).

Microphysical budget computations carried out during the course of the simulations have been used to derive the mean vertical distribution of the hydrometeors and to quantify the relationships among the different water species. In the case of IOP 2A, the upper part of the cloud is composed of ice particles with an increasing degree of riming as the melting level is approached. Pristine ice, snow aggregates, and graupel peak at 10, 9 and 7 km respectively and a thick layer of hail is found above and below the freezing level located at 4 km. At the low levels, liquid precipitation is very intense. Results obtained for IOP 3 are similar but the vertical extent of the cloud being reduced, graupel and hail are present in much smaller amounts. In the case of IOP 8, the vertical structure is quite different. Above the freezing level the cloud is essentially composed of snow aggregates occupying a thin layer less than 2 km deep, and below the freezing level the liquid precipitation is a quarter of that in IOP 2A. All these results are in good agreement with the cloud microphysics retrievals deduced from the S-Pol radar observations.

In terms of microphysical processes, there are some common features to the three IOPs. In the upper part of cloud, autoconversion and aggregation of pristine ice are the most efficient processes to generate solid precipitation, whereas cloud autoconversion and melting provide the main sources of liquid precipitation in the lower part of the cloud. But there are also some marked differences between the three cases. First, the relative contribution of vapour deposition is much larger in IOP 8 than in IOPs 2A and 3. Second, in all three cases, snow riming is present just above the freezing level but the riming processes become really efficient only in the case of IOP 2A, for which heavy riming takes place and transforms snow into graupel. Finally, only in IOP 2A is the wet growth of graupel strong enough to generate the formation of hail in significant amounts.

No major inconsistencies were found between the numerical results and the conceptual models of Medina and Houze. In agreement with Medina and Houze's findings, the numerical results of IOP 8, representative of a blocked stable case, exhibit a shallow stratiform cloud deck in which the dominant ice hydrometeor is snow, efficiently growing by vapour deposition. Also in agreement with the conceptual model of an unblocked unstable situation, the numerical results of IOPs 2A and 3 show much deeper systems in which graupel and its associated growth modes play an important role. However, major differences can still be noted between a case of deep convection (IOP 2A) and a case of moderate convection (IOP 3), as wet growth processes and hail formation only appear in the most convective case. IOP 2A, as the most convective event observed during MAP, and IOP 3, owing to its weak instability, can be viewed as two extreme examples of the unblocked unstable flow prototype in contrast to IOP 2B, which is the most representative example of such a flow. Without questioning the conceptual models of Medina and Houze, it can be mentioned that their representation of unblocked unstable flow might

be too simplistic to adequately describe a deep convective event such as IOP 2A, for which the wet growth processes make a strong contribution and lead to the formation of hail.

ACKNOWLEDGEMENTS

We wish to thank M. Hagen (from DLR), N. Asencio and P. Tabary (from Météo-France), and O. Pujol (from LA) who carried out or contributed to the radar data analysis. This study has been supported by the CNRS/INSU Programme Atmosphère et Océan à Multi-échelles. Computational resources were provided by IDRIS (under project 050569-CP1).

APPENDIX

This appendix provides a short survey of the microphysical schemes sketched in Fig. 2. Additional information can be found in the Meso-NH scientific documentation (http://www.aero.obs-mip.fr/∼mesonh).

Pristine ice is initiated by homogeneous nucleation (HON) when $T \leqslant -35\,°\mathrm{C}$, or more frequently by heterogeneous nucleation (HEN); the small ice crystal concentration depends on the local supersaturation over ice. These crystals grow by water vapour deposition (DEP), as explained below, and by the Bergeron–Findeisen effect (BER). The snow phase is initiated by autoconversion (AUT) of the primary ice crystals. Snow grows by DEP, by aggregation (AGG) through small crystal collection, and by light riming after impaction of cloud droplets (RIM) and of raindrops (ACC). The graupel is produced by the heavy riming of snow (RIM and ACC) or by rain freezing (CFR) when supercooled raindrops come in contact with pristine ice crystals. According to the efficiency of their collecting capacity on the one hand and to a heat balance equation on the other, graupel can grow either in a DRY mode or in a WET mode. The latter occurs when riming is intense enough for part of the collected water to be unable to freeze, leaving the graupel as a hailstone embryo. In this case, the non-freezable water at the surface of the graupel is shed away (SHD) and is converted into raindrops. Both DRY and WET rates are computed but the most limiting one, the lowest rate, is retained in the ICE3 scheme. In the ICE4 scheme, hail is differentiated from graupel. The hail production rate is estimated as proportional to the WET growth rate after normalization by the sum of the DRY and the WET rates. For the sake of simplicity, hail exclusively grows in WET mode and never transforms back into graupel.

When $T \geqslant 0\,°\mathrm{C}$, the pristine crystals immediately melt into cloud droplets (MLT) while the melting snowflakes are simultaneously converted (CVM) into graupel. Graupel and hail particles progressively melt (MLT) into raindrops as they fall. The other (warm) processes are described by the Kessler scheme: autoconversion of cloud droplets (AUT), accretion (ACC) and rain evaporation (EVA). With the exception of cloud droplets, each condensed water species has a substantial fall speed, thus leading to an integrated sedimentation rate (SED).

The coexistence of cloud droplets and small ice crystals in mixed-phase clouds necessitates careful treatment of the fast water vapour exchanges (DEP and CND). This question refers back to the way supercooled water can be available in vigorous convective clouds. As is usually done, a 'floating' saturation vapour mixing ratio, $Rv_{c,i}^{\mathrm{sat}}$, is defined by a barycentric formula using the vapour saturation curves over water and ice and the respective mixing ratios Rc and Ri. In the ICE3/ICE4 schemes, the DEP and CND rates result from an implicit adjustment relative to $Rv_{c,i}^{\mathrm{sat}}$, but with an original

closure where any deficit(excess) of Rv due to the adjustment is directly compensated (absorbed) by the available water phase amount. The adjustment algorithm is non-iterative and second-order accurate.

REFERENCES

Arakawa, A. and Messinger, F. 1976 Numerical methods used in atmospheric models. GARP Tech. Rep. 17, WMO/ICSU, Geneva, Switzerland

Asselin, R. 1972 Frequency filter for time integrations. *Mon. Weather Rev.*, **100,** 487–490

Bechtold, P., Bazile, E., Guichard, F., Mascart, P. and Richard, E. 2001 A mass flux convection scheme for mesoscale and global models. *Q. J. R. Meteorol. Soc.*, **126,** 865–889

Bougeault, P., Binder, P., Buzzi, A., Dirks, R., Houze, R. A., Kuettner, J., Smith, R. B., Steinacker, R. and Volkert, H. 2001 The MAP special observing period. *Bull. Am. Meteorol. Soc.*, **82,** 433–462

Bousquet, O. and Smull, B. F. 2003 Observations and impacts of upstream blocking during a widespread orographic precipitation event. *Q. J. R. Meteorol. Soc.*, **129,** 391–410

Doswell III, C. A., Brooks, H. E. and Maddox, R. A. 1996 Flash flood forecasting: an ingredient-based methodology. *Weather and Forecasting*, **11,** 560–581

Frei, C. and Häller, E. 2001 'Mesoscale precipitation analysis from MAP SOP rain-gauge data'. Pp. 257–260 in MAP Newsletter No. 15. MeteoSwiss, CH-8044, Zurich, Switzerland

Gal-Chen, T. and Sommerville, C. J. 1975 On the use of a coordinate transformation for the solution of the Navier–Stokes equations. *J. Comput. Phys.*, **17,** 209–228

Germann, U. and Joss, J. 2000 'Spatial continuity of Alpine precipitation'. P. 20 in proceedings of the MAP meeting 2000, 24–26 May 2000, Bohinjska Bistrica, Slovenia

Hagen, M. 1999 'The Alpine radar composite'. Pp. 20–21 in MAP Newsletter No. 11. MeteoSwiss, CH-8044, Zurich, Switzerland

Houze, R. A., James, C. N. and Medina, S. 2001 Radar observations of precipitation and airflow on the Mediterranean side of the Alps: Autumn 1998 and 1999. *Q. J. R. Meteorol. Soc.*, **127,** 2537–2558

Houze, R. A. and Medina, S. 2005 Turbulence as a mechanism for orographic precipitation enhancement. *J. Atmos. Sci.*, IMPROVE special issue, **62,** 3599–3623

Keil, C. and Cardinali, C. 2004 The ECMWF re-analysis of the Mesoscale Alpine Programme Special Observing Period. *Q. J. R. Meteorol. Soc.*, **130,** 2827–2850

Lafore, J. P., Stein, J., Asencio, N., Bougeault, P., Ducrocq, V., Duron, J., Fisher, C., Héreil, P., Mascart, P., Masson, V., Pinty, J.-P., Redelsperger, J.-L., Richard, E. and Vilà-Guerau de Arellano, J. 1998 The Meso-NH atmospheric simulation system. Part I: Adiabatic formulation and control simulations. *Annales Geophysicae*, **16,** 90–109

Lascaux, F., Richard, E., Keil, C. and Bock, O. 2004 Impact of the MAP reanalysis on the numerical simulation of the MAP-IOP 2A convective system. *Meteorol. Z.*, **13,** 49–54

Lipps, F. and Hemler, R. S. 1982 A scale analysis of deep moist convection and some related numerical calculations. *J. Atmos. Sci.*, **39,** 2192–2210

Massacand, A. C., Wernli, H. and Davies, H. C. 1998 Heavy precipitation on the Alpine southside: An upper-level precursor. *Geophys. Res. Lett.*, **25,** 1435–1438

Medina, S. and Houze, R. A. 2003 Air motions and precipitation growth in Alpine storms. *Q. J. R. Meteorol. Soc.*, **129,** 345–371

Pinty, J.-P. and Jabouille, P. 1998 'A mixed-phase cloud parameterization for use in a mesoscale non hydrostatic model: Simulations of a squall line and of orographic precipitation'. Pp. 217–220 in Proceedings of Conference on Cloud Physics, 17–21 August 1998, Everett, USA

Pinty, J.-P., Richard, E. and Tabary, P. 2002 'Fine-scale simulations of the MAP-IOP 2A precipitating system: comparison with radar data and sensitivity to the hail category'. Proceedings of Conference on Cloud Physics, 3–8 June 2002, Ogden, USA

Pujol, O., Georgis, J.-F., Chong, M. and Roux, F. 2005 Dynamics and microphysics of orographic precipitation during MAP IOP 3. *Q. J. R. Meteorol. Soc.*, **131,** 2795–2819

Richard, E., Cosma, S., Tabary, P. and Hagen, M. 2001 'High-resolution numerical simulation of the squall line observed during MAP IOP 2a'. Pp. 53–56 in MAP Newsletter No. 15. MeteoSwiss, CH-8044, Zurich, Switzerland

Richard, E., Cosma, S., Tabary, P., Pinty, J.-P. and Hagen, M. 2003 High-resolution numerical simulations of the convective system observed in the Lago Maggiore area on 17 September 1999 (MAP IOP 2A). *Q. J. R. Meteorol. Soc.*, **129,** 543–564

Richard, E., Buzzi, A., Zängl, G., Ascencio, N., Benoit, R., Chiao, S., Ferretti, R., Hohenegger, C., Keil, C., Lin, Y.-L., Marsigli, C., Medina, S. and Schär, C. 2005 'Quantitative precipitation forecasting in mountainous regions—pushed ahead by MAP'. Pp. 65–69 of Proceedings of ICAM/MAP 2005, Zadar, Croatia, 23–27 May 2005. Available at http://meteo.hr/ICAM2005/proceedings.html

Rotunno, R. and Ferretti, R. 2003 Orographic effects on rainfall in MAP cases IOPs 2b and 8. *Q. J. R. Meteorol. Soc.*, **129,** 373–390

Stein, J., Richard, E., Lafore, J. P., Pinty, J.-P., Asencio, N. and Cosma, S. 2000 High-resolution non-hydrostatic simulations of flashflood episodes with grid nesting and ice phase parameterization. *Meteorol. Atmos. Phys.*, **72,** 203–221

Steiner, M., Bousquet, O., Houze, R. A., Smull, B. F. and Mancini, M. 2003 Airflow within major Alpine river valleys under heavy rainfall. *Q. J. R. Meteorol. Soc.*, **129,** 411–432

Tabary, P., Scialom, G., Richard, E., Seity, Y. and Soula, S. 2002 'Orogenic squall line observed with Doppler polarimetric data during the MAP experiment'. Proc. of 10th Conference on Mountain Meteorology and MAP meeting, 17–21 June 2002, Park City, USA

Vivekanandan, J., Zrnic, D., Ellis, S., Oye, R., Ryzhkov, A. and Straka, J. 1999 Cloud microphysics retrieval using S-band dual-polarization radar measurements. *Bull. Am. Meteorol. Soc.*, **80,** 381–387

Volkert, H. 2005 'The Mesoscale Alpine Programme (MAP): A multi-faceted success story'. Pp. 226–230 of Proceedings of ICAM/MAP 2005, Zadar, Croatia, 23–27 May 2005. Available at http://meteo.hr/ICAM2005/proceedings.html